The effect of B-site order-disorder in the structure and magnetism of the new perovskite family $La_2MnB'O_6$ with B' = Ti, Zr and Hf

Diana M. Arciniegas Jaimes[a, #], Juan M. De Paoli[a,f], Vivian Nassif[b], Paula G. Bercoff[c,f], Germán Tirao[c,f], Raúl E. Carbonio[a,f] and Fernando Pomiro[d,a *]

[a] *INFIQC (CONICET – Universidad Nacional de Córdoba), Departamento de Fisicoquímica, Facultad de Ciencias Químicas, Universidad Nacional de Córdoba, Haya de la Torre esq. Medina Allende, Ciudad Universitaria, X5000HUA Córdoba, Argentina.*
[b] *UGA, CNRS, Institut Néel, 38000 Grenoble, France.*
[c] *IFEG CONICET, Facultad de Matemática, Astronomía, Física y Computación, Universidad Nacional de Córdoba, Av. Medina Allende s/n, 5000, Córdoba, Argentina.*
[d] *Department of Chemistry, University of Warwick, Gibbet Hill, Coventry, CV4 7AL, United Kingdom.*
[f] *Researchers of CONICET.*

Keywords: Perovskites, Neutron powder diffraction, Anti-site disorder effects, Symmetry-adapted refinements, Magnetic structures, Antiferromangnetism, Spin-glass.

Abstract

In this work we report the synthesis as well as the structural and magnetic characterisation of the three perovskites $La_2MnB'O_6$ (B'= Ti, Zr and Hf). Interestingly, only La_2MnTiO_6 crystallizes in the monoclinic double perovskite space group $P2_1/n$, with complete rocksalt order of the B-site cations, whereas La_2MnZrO_6 and La_2MnHfO_6 crystallize in the orthorhombic simple perovskite space group *Pbnm*, with complete disorder in the B-site. Moreover, the magnetic susceptibility at low temperatures shows clear antiferromagnetic transitions below 10 K for the three compounds, but only the Ti-based perovskite has long-range magnetic ordering. The latter compound has an antiferromagnetic Type-II structure described by the P_{S-1} magnetic space group while the other two have a spin-glass behaviour below the transition temperature due to both spin disorder and competing superexchange interactions in the systems. This is the first time that two of the three studied compounds were synthesized (B'= Zr and Hf) and the first time that the whole series is described in thorough detail using symmetry-adapted refinements and magnetic crystallography.

* Corresponding author
e-mail: fpomiro@fcq.unc.edu.ar (F. Pomiro)
#Current affiliation: *IFEG CONICET, Facultad de Matemática, Astronomía, Física y Computación, Universidad Nacional de Córdoba, Av. Medina Allende s/n, 5000, Córdoba, Argentina.*

1. Introduction

Perovskites are very attractive materials due to their interesting physical properties and broadly extended fields of applications such as catalysis,[1] multiferroism,[2] oxygen transport,[3] magnetoresistivity,[4] among others. The general formula of the perovskite structure is ABX_3 (where A and B are cations with different oxidation states and X is an anion) and it is highly flexible in accommodating almost all the elements of the periodic table in its A and B sites.[5] The three-dimensional array of the perovskite consists of corner-sharing octahedra BO_6 with the A cations in the twelve-fold cavities in between the BO_6 octahedra. Many different structural distortions have been observed in perovskites but one of the most important is the tilting of the octahedra due to small cations placed in the A site of the structure.[6]

When two different cations are placed in the B sites of the perovskite, two possible scenarios emerge, depending on the difference in size and charge of those two cations[7] (also other factors are determinant, such

as synthesis conditions[8]). If the two species are of similar size and charge, they are likely to be distributed over the octahedral sites in a disordered manner; otherwise, they may order (e. g. in a rocksalt manner), therefore doubling the size of the unit cell. In the latter case, the general formula is $A_2BB'O_6$ and the structure is called double perovskite. The degree of disorder (or anti-site disorder, ASD), affects several of the physical properties observed in double perovskites, for example in Sr_2FeMoO_6[9] and Pb_2ScTaO_6,[10] in which the magneto-transport and the dielectric properties, respectively, are intensely affected by the degree of ASD in the perovskite. The existence of ASD in the B sublattice gives rise also to unusual magnetic properties, for example, competing superexchange interactions lead to a spin–glass behaviour in Sr_2FeRuO_6 and $BaLaNiRuO_6$.[11] By contrast, in ordered perovskites such as Ba_2NdRuO_6[12] and Sr_2HoRuO_6[13] a long-range antiferromagnetic ordering was found, involving Ru^{5+} and Nd^{3+}, or Ho^{3+}, respectively.

It is important mentioning that in a double perovskite $A_2BB'O_6$, each B cation forms a pseudo face-centred cubic (*fcc*) sublattice in which, when only B' is a diamagnetic cation, two types of magnetic interactions can be present (see **Figure 1)**: a) between nearest-neighbour (NN) cations, J_{NN}, with a B-O-O-B path and b) between next-nearest-neighbours (NNN) cations, J_{NNN}, with B-O-B'-O-B path.[14] Due to the above, there are three possible antiferromagnetic (AFM) orderings which depend on the strengths of the J_{NN} and J_{NNN} interactions, namely Type I ($J_{NN} >>> J_{NNN}$), Type II ($J_{NN} < J_{NNN}$) and Type III ($J_{NN} > J_{NNN}$).[14] On the other hand, in disordered perovskites containing one or more magnetic cations, there is an important competition between the different superexchange interactions in the system giving rise to possible spin-glass behaviour.[15, 16]

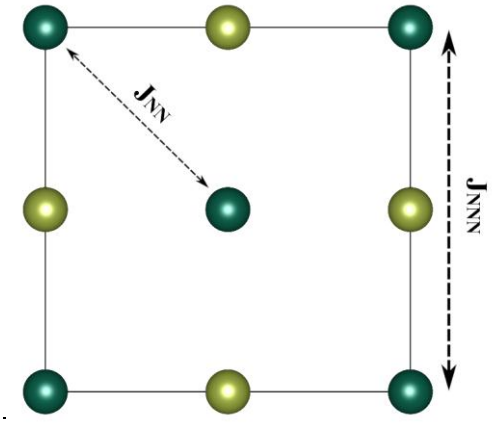

Figure 1. Schematic view of the different magnetic interactions in a double perovskite when one of the two B-sites is occupied with diamagnetic cations. The dark- and light-green spheres represent the magnetic and diamagnetic cations, respectively. J_{NN} and J_{NNN} are the nearest-neighbour and next-nearest-neighbour interactions, respectively.

Herein, the synthesis of the three perovskites $La_2MnB'O_6$ (B'= Ti, Zr and Hf) is reported, two of them for the first time in the literature.[17] We performed symmetry-adapted refinements in the neutron powder diffraction (NPD) data collected at 300 K as well as a detailed comparison among the distortions observed in the three samples. We found that the Ti-based compound crystallizes in the common monoclinic double perovskite space group $P2_1/n$, in contrast with previous works in which only X-ray powder diffraction is used for characterization,[18, 19] whereas the Zr- and Hf-based samples crystallize in the common orthorhombic simple perovskite space group *Pbnm*. The three perovskites show an AFM transition below 10 K but only the Ti-based sample displays long-range magnetic ordering. The magnetic space group of the Ti-based sample is P_{S-1} (number 2.7) and corresponds to an AFM Type-II magnetic structure, in which $J_{NNN} > J_{NN}$. On the other hand, spin-glass-like behaviour was found in the Zr- and Hf-based samples.

2. Experimental section

2.1 Samples preparation

Polycrystalline powder samples of $La_2MnB'O_6$ (B'= Ti, Zr and Hf) were synthesized using a conventional solid-state chemistry method, starting from the following reagents as powders in analytical grade: La_2O_3 (pre-dried at 1173 K), MnO, TiO_2, ZrO_2 and HfO_2.

For the synthesis of the Zr-based perovskite, stoichiometric quantities of the regents were mixed in an agate mortar in a first stage. Then, the powder was pelletized and calcined at 1623 K for 12 h under high-purity argon flux with titanium getter, which removes most of the residual O_2 inside the tube furnace. The identified phases after this thermal treatment were a perovskite phase that may correspond to La_2MnZrO_6 (about 66%), a pyrochlore phase that may correspond to $La_2Zr_2O_7$ (about 11%) and unreacted La_2O_3 (about 23%). After several thermal treatments, we noticed that both the increase of the time at 1623 K and the increase of the temperature in the thermal treatments stabilised the pyrochlore phase $La_2Zr_2O_7$ rather than the perovskite (see **Figure S1** in the Supporting Information (SI)). This is because pyrochlore phases are kinetically favourable and it is very difficult to achieve their complete elimination under these synthesis conditions.[20] Since we did not observe any traces of unreacted MnO after the thermal treatments, we decided to test if the perovskite phase stabilises with MnO excess. To test this hypothesis, the precursors were prepared with 5%, 10%, 15% and 20% MnO excess and, after mixing and pelletizing, the samples were heated at 1623 K for 12 h under high-purity argon flux with Ti getter. The powder prepared with a 20% MnO excess was highly pure, reaching 98% of La_2MnZrO_6. The same procedure was followed for the preparation of Ti- and Hf- based perovskites, with a MnO excess of 5% and 10%, respectively, used to obtain the purest samples. There might be two possible explanations to this experimental fact: 1) MnO reacts with alumina from the crucible; 2) MnO volatilizes. Reaction with the crucible is thoroughly informed for CoO (crucibles turn blue in colour, which is the colour of the Co doped alumina), however we did not observe changes in the colour of the alumina crucible after the reaction. On the other hand, MnO has been shown to be volatile between 850^o C and 1050^o C.[21] It is sensible to think that volatilization increases with temperature and therefore at 1350^o C MnO might volatilize.

For B'= Zr, secondary phases La_2O_3 (0.6%) and $La_2Zr_2O_7$ (1.73%) were detected whereas for B'= Hf only a minor amount of $La_2Hf_2O_7$ (5%) was identified. On the other hand, for B'= Ti we did not detect any impurity phase from the X-ray powder diffraction (XRPD) data. However, as we explain later, there are very small amounts of MnO present in the Ti- (~0.3 %) and Zr-based (~0.8 %) samples, which we were able to identify by analysing the magnetic reflections observed in the NPD data at low temperature.

2.2 X-ray powder diffraction, neutron powder diffraction, Rietveld analysis and scanning electron microscopy

XRPD patterns were measured at room temperature (RT) with a PANalytical X'Pert Pro diffractometer (40 kV, 40 mA) in Bragg–Brentano geometry with Cu Kα radiation (λ= 1.5418 Å) using a PIXcel 1D detector. They were recorded between 10-120° in 2θ, with a step size of 0.02° and 10 s for step counting time. The samples were placed on a zero-diffraction Si single crystal sample holder. NPD patterns were collected in the D1B powder diffractometer (λ= 2.52 Å and 1.28 Å) at the Institute Laue-Langevin (ILL) at temperatures between 300 and 2 K. They were recorded between 0.77-128.67° in 2θ, with a step size of 0.1°. Crystalline and Magnetic Structure refinements of the XRPD and NPD patterns were performed with the Rietveld method[22] using FullProf[23] and Topas with the JEDIT interface,[24] and VESTA[25] software was used for visualization of the crystal and magnetic structures. The refined parameters were: background, scale factor, zero shift, cell parameters, atomic positions, occupancies, isotropic atomic displacement parameters, as well as the usual profile parameters describing the peak shape functions.

A Σigma Carl Zeiss field-emission scanning electron microscope (FE-SEM) with an attached Oxford detector for energy dispersive spectroscopy (EDS) was employed at 5 keV and 20 keV to perform the morphological and semi-quantitative chemical characterization, respectively.

2.3 X-Ray Emission Spectroscopy

High-resolution Kβ X-Ray Emission Spectroscopy **(**XES) spectra of La_2MnZrO_6 and the standards (MnO, Mn_2O_3, MnO_2 and a related perovskite $BaLaMnSbO_6$) were measured using a non-conventional spectrometer[26] based on quasi-back-diffraction geometry. The measurements were performed in a conventional 45°-45° geometry and the whole spectrum from a cobalt-target X-ray tube, operated at 40 mA and 37 kV, was used as an irradiation source. High resolution Kβ emission spectra were recorded by scanning, in steps of 0.2 eV around the $K\beta_{1,3}$ main line, the analyser and the detector synchronously.

2.4 Magnetic Measurements

Magnetic measurements were conducted using a commercial MPMS XL 7 T superconducting quantum interference device magnetometer (SQUID), on compacted powdered samples, from 2 K to 350 K at 100 Oe in zero-field cooling/field cooling (ZFC-FC) modes. Isothermal magnetization loops were performed in a wide range of temperatures with a maximum applied field of 20 kOe.

3. Results and Discussion

The XRPD data collected at RT for $La_2MnB'O_6$ (B'= Zr, Ti and Hf) display high crystallinity and purity in the three samples (see **Figure S2** in SI). The crystal structures for $La_2MnB'O_6$ (B'= Ti, Zr and Hf) were refined using the NPD data measured at 300 K with λ = 1.28 Å. The refined NPD patterns for the three samples are shown in **Figure 2**. The sample with B'=Ti was refined with the common monoclinic double perovskite space group $P2_1/n$ (number 14), where the symmetry comes from the combination of octahedral tilting described by the Glazer tilt system[6] $a^-a^-c^+$ and rocksalt ordering of the octahedral cations Mn^{2+} and Ti^{4+} (see **Figure 3a**). The rocksalt ordering observed in this sample through the analysis of the NPD patterns differs from what was previously reported using XRPD by Ramanujachary[19] and Kagemashira,[18] where a disordered orthorhombic structure was proposed. In our case, it was impossible to detect any ordering feature in the XRPD data and the NPD data was key to determine the rocksalt ordering between Mn and Ti in the structure (see **Figure S3a** in the SI). In the case of the samples with B'=Zr and Hf, the crystal structures were refined in both cases with the common orthorhombic simple perovskite space group *Pbnm* (number 62), which share the same octahedral tilting pattern ($a^-a^-c^+$ in the Glazer notation) than $P2_1/n$ (see **Figure 3a**) but with a total ASD of the cations on the B-sites of the perovskite structure (see **Figure S3b** in the SI). In **Table 1** the cell parameters, refined stoichiometry and agreement factors are displayed. In addition, the .cif files of the final refinements for the three samples are provided as separate files in the SI. Also, atomic coordinates, thermal parameters and occupancies for the whole family after the Rietveld refinement of the NPD data at 300 K are displayed in **Table S1**.

The difference observed in the ordering of the B-site cations among the different members of the family might be explained by the radii difference (Δr) between the B ($r(Mn^{2+}{}_{HS})_{oh}$= 0.83 Å) and B' ($r(Ti^{4+})_{oh}$= 0.605 Å, $r(Zr^{4+})_{oh}$= 0.72 Å and $r(Hf^{4+})_{oh}$= 0.71 Å)[27] cations in the samples. The Δr for the Ti-, Zr- and Hf-based perovskites are 0.225 Å, 0.11 Å and 0.12 Å, respectively. The Δr for the Ti-based sample is slightly bigger than the lower limit (Δr > 0.2 Å) in which a perovskite structure has a high probability to present cationic ordering.[7] Since the difference in charge between B and B' is about the same in the three samples (Δq= 2), the radii mismatch in the Ti-based compound explains the rocksalt ordering observed in this case.

Table 1. Unit-cell parameters, cell volume, agreement factors and final stoichiometry after the Rietveld refinement using NPD data at 300 K for Ti-, Zr- and Hf-based perovskites.

	B'=Ti	**B'=Zr**	**B'=Hf**
Space group	***P2$_1$/n (#14)***	***Pbnm* (#62)**	***Pbnm* (#62)**
***a* (Å)**	5.6130(3)	5.6930(3)	5.6992(3)
***b* (Å)**	5.7006(3)	5.8831(3)	5.8799(3)
***c* (Å)**	7.9724(5)	8.1313(5)	8.1381(4)
***β* (°)**	89.93(1)	90	90
***V* (Å^3)**	255.10(3)	272.34(3)	272.71(4)
***R$_p$* (%)**	7.01	6.06	6.82
***R$_{wp}$* (%)**	6.59	6.60	6.32
***R$_{exp}$* (%)**	0.96	0.87	0.90
***R$_{Bragg}$* (%)**	2.11	2.87	2.71
Final refined stoichiometry	$La_{1.96(1)}[Mn_{0.99(1)}Ti_{0.01(1)}]^{B}[Ti_{0.99(1)}Mn_{0.01\,(1)}]^{B'}O_{5.95(1)}$	$La_{0.99(1)}Mn_{0.52(1)}Zr_{0.48(1)}O_{2.99(1)}$	$La_{0.98(1)}Mn_{0.51(1)}Hf_{0.49(1)}O_{2.99(1)}$

According to the final stoichiometry obtained after the occupancies refinements (see **Table 1),** La^{3+} and O^{2-} vacancies for the Ti-based perovskite (about 2.5% and 0.83%, respectively) can be noticed. If we consider that Ti remains with an oxidation state of 4+, this corresponds to a Mn oxidation state of +2.05 (95% of Mn^{2+} and 5% of Mn^{3+}). Less La^{3+} vacancies were observed in La_2MnZrO_6 and La_2MnHfO_6 together with a slightly higher amount of Mn in the B-site of the perovskite for both samples. This observation is in perfect agreement with the small percentage of the phase $La_2B'_2O_7$ (B'= Zr and Hf) detected as an impurity in the synthesis of these compounds. The Mn oxidation states calculated from the obtained formulas are +2.22 (86.5 % of Mn^{2+} and 13.5% of Mn^{3+}) and +2.20 (84.3 % of Mn^{2+} and 15.7% of Mn^{3+}) for the Zr- and Hf-based samples, respectively.

To double-validate the oxidation state of Mn obtained from the analysis of NPD data, we decided to perform high-resolution Kβ emission measurements in one member of the family, the Zr-based compound, because it has the highest oxidation state value of Mn obtained through NPD. For this reason, high-resolution Kβ emission spectra of La_2MnZrO_6 were measured together with those for mixed manganese oxides (MnO, Mn_2O_3 and MnO_2) and the double perovskite $BaLaMnSbO_6$,[28] whose oxidation states are known, and therefore, could be used as standards (further details are presented in the SI, **Figures S4a** to **S4c**). From this analysis, it was obtained that the average oxidation state of Mn in the perovskite $La_{0.99(1)}Mn_{0.52(1)}Zr_{0.48(1)}O_{3.00}$ is (2.10 ± 0.11), which is in very good agreement with the value obtained from the analysis of NPD data. Both techniques agree in that a small amount of the Mn in the Zr-based perovskite is Mn^{3+}.

The particle size and morphology of the three new perovskites were explored by SEM. All the members of the family are composed by well-defined crystals with granular topology containing different grain sizes homogeneously distributed throughout the samples (see **Figure S5a** in SI as a representative image for the whole family). In addition, through the XRPD data, the coherently scattering domain size were obtained using the Scherrer's equation[29] with the most intense peaks in the diffraction patterns. The coherently scattering domain size for the Ti-, Zr- and Hf-based compounds are 63 nm, 79 nm and 66 nm, respectively. The values obtained with Scherrer's formula are estimative of the crystallite sizes, which in our perovskites are smaller than particle sizes (see **Figure S5a**) as usually observed in polycrystalline samples. In addition, EDS scanning map shown in **Figure S5b** displays the element compositions of the as-prepared B'= Zr perovskite. The different colour spots over the dark background display a uniform distribution of the elements on the external surface of the particles.

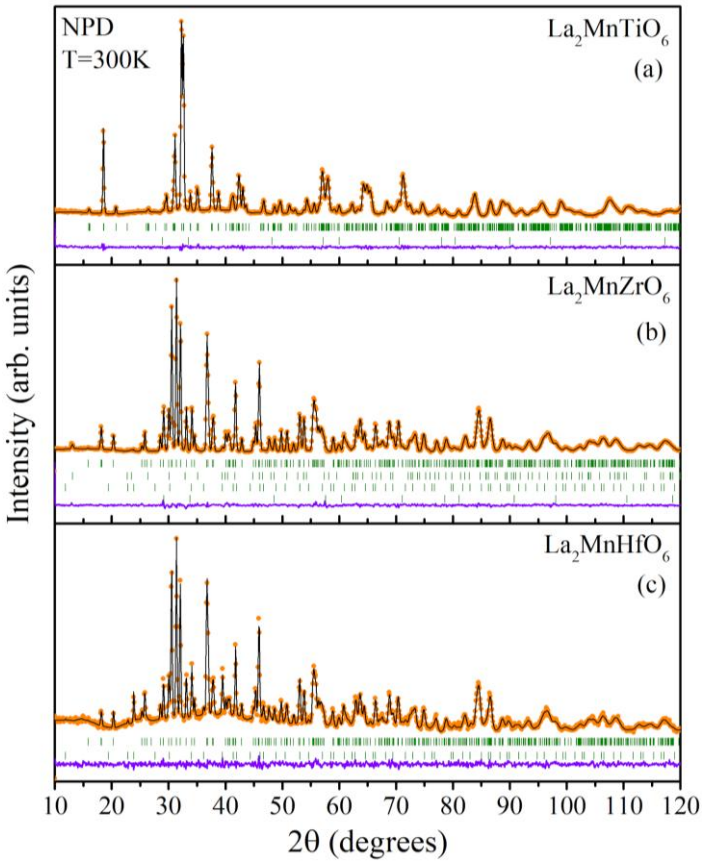

Figure 2. Refined NPD patterns collected at 300 K with λ= 1.28 Å for **(a)** B'= Ti, **(b)** B'= Zr and **(c)** B'= Hf. Observed (orange dots), calculated (black solid line), Bragg reflections (vertical green bars) and difference (blue bottom line). The first set of Bragg reflections corresponds to the reflections of the main perovskite phase. The second set of reflections in **(a)** corresponds to unreacted MnO. The second, third and fourth set of reflections in **(b)** correspond to La_2O_3, $La_2Zr_2O_7$ and MnO, respectively. The second set of reflections in **(c)** corresponds to $La_2Hf_2O_7$.

In order to compare the structural distortions observed in the three new perovskites, we performed symmetry-adapted refinements using the NPD data collected at 300 K. We used the web-based tool ISODISTORT[30] to generate the child structure parametrized in terms of distortion modes that may be readily refined with the Rietveld refinement program TOPAS. $P2_1/n$ basis = (-1, 0, 1), (-1, 0, -1), (0, -2, 0), origin = (0,1/2,0) was generated from the parent *Pm-3m* structure with setting *A 1b* (½, ½, ½); *B 1a* (0, 0, 0); X *3d* (½, 0, 0) (the .inp file obtained from ISODISTORT and the **Table S2** with a comparison of the Irreps's notations generated with the perovskite setting *A 1a (0, 0, 0)*; *B 1b (½, ½, ½)*; *X 3c (0, ½, ½)* are included in the SI). This model has twelve degrees of freedom (or distortion modes) corresponding to eight different Irreducible representations (Irreps) labelled R_5^+, X_5^+, R_1^+, R_4^+, M_3^+, R_3^+, M_2^+ and M_5^+. The first character of the label is a capital letter that represents the position of the Brillouin zone (BZ) of the parent structure to which it belongs, a sign indicating the conservation (+) or violation (−) of parity with respect to the inversion centre at the origin of the unit cell, and a number corresponding to the tabulation by Stokes and Hatch.[30] The R_4^+ and M_3^+ modes correspond to octahedral tilts, the former is an out-of-phase octahedral tilting in the *a*-*b* plane ($a^-a^-c^0$ in the Glazer notation[6]) and the last is an in-phase octahedral tilt about the *c*-axis ($a^0a^0c^+$). Schematic representations of these two distortions are shown in **Figure 3a**. The R_1^+ mode corresponds to a breathing distortion of the oxygens that is related to the rocksalt ordering of the B-site cations (it is also represented in **Figure 3a**). The rest of the modes are related to anti-polar distortions ($R_5^+$and X_5^+), Jahn-Teller distortions (R_3^+ and M_2^+) and basal oxygen rotation around the *a*-axis (M_5^+),which are described in more detail in literature[31-33].

In the case of the *Pbnm* model, only seven out of the twelve distortion modes present in $P2_1/n$ are allowed, corresponding to five different Irreps, namely–R_5^+, X_5^+, R_4^+, M_3^+ and M_2^+. **Figure 3b** compares the mode amplitudes obtained for each sample after the symmetry-adapted refinements using the NPD data collected at 300K.

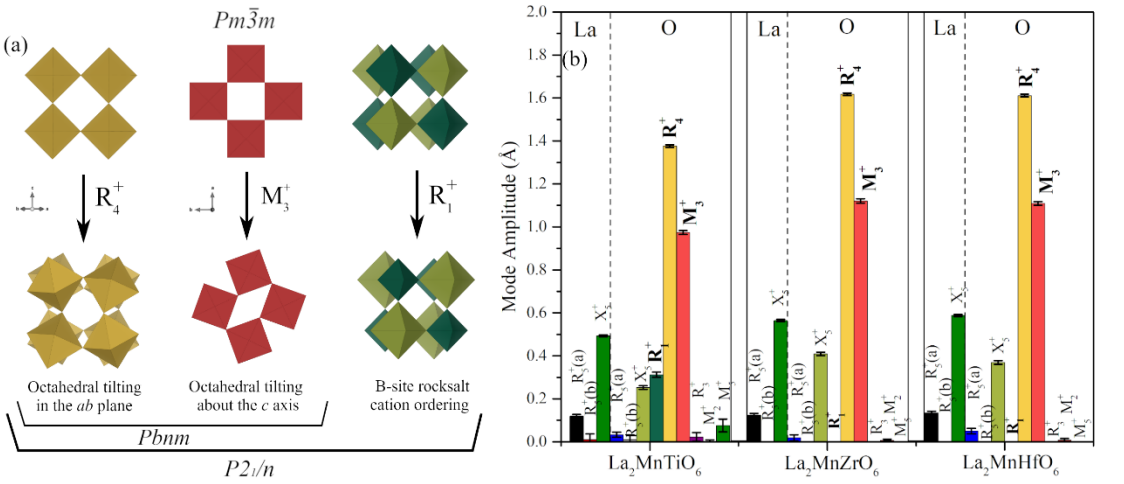

Figure 3. **(a)** Schematic representation of the most important distortions observed in the analysed structures. **(b)** Mode amplitudes obtained after the symmetry-adapted refinement performed using the NPD data collected at 300 K for $La_2MnB'O_6$ (B'= Ti, Zr and Hf).

We can see from **Figure 3b** that the most important modes in the three structures are the R_4^+ and M_3^+, both of them with a larger mode amplitude in the Zr- and Hf-based samples than in the Ti-based one. As we mentioned before, those modes correspond to the out-of-phase octahedral tilting in the *a-b* plane and the in-phase octahedral tilting about the *c*-axis, respectively (see **Figure 3a**). It is worth noting that for the *Pbnm* structures, the specific superposition of the appropriate R_4^+ and M_3^+order parameters is primary (i.e., solely responsible for breaking the symmetry of the *Pm-3m* parent) as was previously reported.[34] The other mode that presents an important amplitude value in the three structures is the anti-polar distortion X_5^+, which arises as second-order parameter of the tilts acting as primary order parameters of the parent *Pm-3m* structure symmetry-breaking (trilinear coupling $R_4^+ \oplus M_3^+ \oplus X_5^+$[33]). One mode that is symmetry-allowed in the $P2_1/n$ space group, and has the largest amplitude for modes not present in *Pbnm*, is the R_1^+ (B-site rocksalt order represented in **Figure 3a**). This mode, together with R_4^+ and M_3^+, is a primary distortion mode in the hypothetical phase transition from *Pm-3m* to $P2_1/n$. From this analysis, we can observe that the tilts that appear in the Zr- and Hf-based samples are slightly larger than those observed in the Ti-based sample, denoting a more distorted structure in the first two mentioned compounds.

In order to evaluate the internal distortions of the octahedra, the distortion parameter, Δd, was calculated according to the following equation at 300 K,

$$\Delta d = \frac{1}{6}\sum_{1}^{6}\left[\frac{d_i - \langle d \rangle}{\langle d \rangle}\right]^2 \qquad (1)$$

where d_i are the individual B-O distances and $<d>$ is the average value of those distances. The refined bond distances, B/B'-O, and also the B-O-B' angles and tilt angles (δ) at RT for the whole family of perovskites are shown in **Table S3**. Distortion values Δd should be zero if the octahedra were perfectly symmetrical and greater than zero if they were distorted. The calculated values of Δd are displayed in **Table 2**. For B'= Ti the Δd values indicate that the TiO_6 octahedra (B'-site) have an internal distortion slightly greater than the MnO_6 (B-site), which might be due to a small cooperative second-order Jahn-Teller distortion produced by the presence of Ti^{4+} (d^0).[35, 36] The distortions observed in the B'-site for La_2MnTiO_6 are not as big as those observed in other systems containing this cation,[35] which might be related to the large octahedral tilting

observed in this sample.[37] On the other hand, the Δ*d* values for Zr- and Hf- based perovskites are lower than those corresponding to site B' in the Ti-based compound, despite both are d^0 cations. This might be because these cations are weaker distorters as compared to the moderate distorter Ti^{4+}.[38]

Table 2. Average octahedral distortions Δ*d* calculated from Eq. (1) at 300K for $La_2BB'O_6$ with B= Mn and B'= Ti, Zr and Hf.

B'	Δ*d* (10^{-5})	
	Site B'	***Site B***
Ti	2.53(2)	2.06(3)
Zr	2.32(3)	
Hf	1.68(2)	

DC susceptibility χ=M/H (being M the magnetization and H the applied magnetic field) as a function of temperature was measured for the prepared perovskites following the zero field cooling-field cooling (ZFC-FC) protocol, between 2 K and 300 K. In ZFC, the system is cooled from room temperature down to 2 K with no applied magnetic field (H= 0). A magnetic field of constant value is then turned on at 2 K and the values χ(T) are registered while warming the system up to 300 K. For measuring the FC curve, the process is repeated while keeping the applied field on, cooling from 300 K to 2 K. The χ(T) values in FC mode are also recorded in warming.

The low-temperature region of the ZFC-FC curves measured with an applied magnetic field of 100 Oe for $La_2MnB'O_6$ (B'= Ti, Zr and Hf) are presented in **Figure 4.** These curves show that the critical temperatures (T_N) for the three samples are very similar, being 9 K for both La_2MnTiO_6 and La_2MnZrO_6, and 7 K for La_2MnHfO_6.

In the case of the Ti-based perovskite, no difference between the ZFC and FC curves can be observed in the whole temperature range (see **Figure 4a**), suggesting the absence of spin-glass behaviour in this compound.[39] Furthermore, the drop in χ(T) below T_N indicates strong antiferromagnetic (AFM) interactions. The low-temperature upturn in the magnetic susceptibility data might be due to the small traces of paramagnetic Mn^{3+} found in the sample (about 5%) or to other paramagnetic impurities not detected in our diffraction experiments.

On the other hand, the irreversibility between the ZFC and FC curves below T_N for the Zr- and Hf-based compounds (see **Figures 4b** and **4c**) can be understood considering a spin-glass-like behaviour in these perovskites, which is reasonable, given the high degree of disorder detected in both samples.

The Curie–Weiss (C-W) fits of the inverse susceptibility in the paramagnetic region (see insets in **Figure 4**) reveal an antiferromagnetic nature of the interaction between the magnetic ions in every case, with negative Curie-Weiss temperatures θ_{C-W} of -26.80 K, -30.42 K and -49.90 K for the Ti-, Zr- and Hf-based perovskites, respectively. The effective magnetic moments obtained from the C-W fittings are 5.87, 5.50 and 5.63 μ_B/f.u. for the Ti-, Zr- and Hf-based compounds, respectively, in very good agreement with Mn^{2+} ions in high-spin configuration equal to 5.92 μ_B.

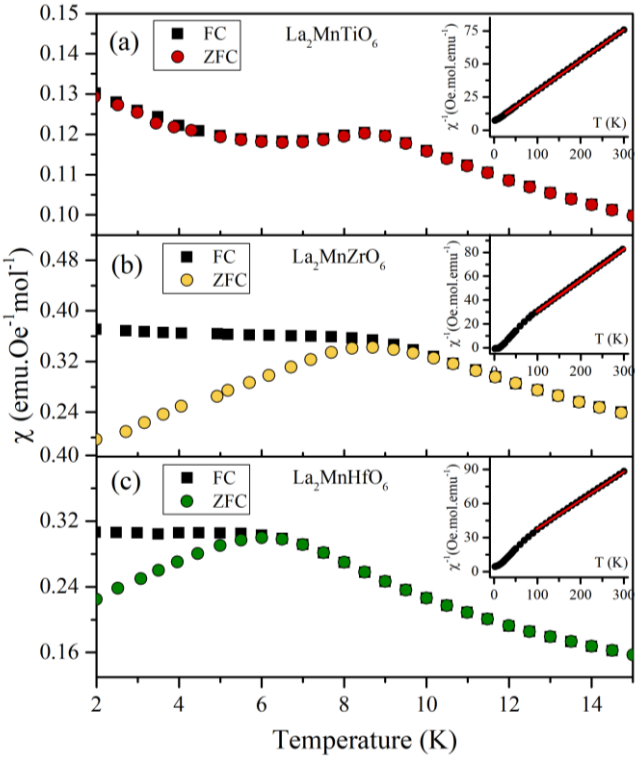

Figure 4. Low temperature region of the M/H vs T curves in ZFC-FC modes for perovskites with B' as **(a)** Ti, **(b)** Zr and **(c)** Hf collected at 100 Oe. The insets show the C-W fits (red line) of the inverse susceptibility in the paramagnetic region.

Isothermal magnetization curves were measured at different temperatures for the three samples with a maximum applied field of 20 kOe. The data corresponding to the first quadrant of the curves are displayed in **Figure 5** together with close-up views of the hysteresis loops in the low-field region in their corresponding insets (see also **Figure S6** in SI). For the Ti-based perovskite, the magnetization loops display no hysteretic behaviour in the whole temperature range (see inset in **Figure 5a** and **Figure S6** in SI). In this compound, the values of magnetization reached at the highest applied magnetic field (20 kOe) are lower than those reached in the Zr- and Hf-based samples. This behaviour in the M vs H curves for the Ti-based perovskite can be associated with the AFM ordering of the Mn cations' magnetic moments (this behaviour will be explained later).

On the other hand, a clear nonlinear M vs H behaviour is observed for the Zr- and Hf-based compounds below T_N, whit a notorious hysteretic behaviour observed at 4 K (see inset in **Figure 5a** and **Figure S6** in SI). This might be understood as a complex behaviour that includes non-compensated AFM (or wFM) order of the Mn cations. The differences observed in the magnetization curves between the Ti-based sample and those with Zr and Hf are mainly due to the existence of ASD in the last two perovskites. As we mentioned in the Introduction, in a double perovskite structure $A_2BB'O_6$, with complete rocksalt order in the B-site and without ASD, B and B' cations form a pseudo *fcc* sublattice. In the cases in which B' is a diamagnetic (or d^0) cation, two types of magnetic interactions are present: through the B-O-O-B path (J_{NN}) and through the B-O-B'-O-B path (J_{NNN}), as shown in **Figure 1**. This is the case for La_2MnTiO_6, where we found complete rocksalt order between Mn and Ti. In the Zr- and Hf-based perovskites we observed total ASD between the two cations in the B-site, which means that the cations are randomly accommodated in the site and therefore the interactions through the Mn-O-Mn paths are also possible. In this case-scenario there might be rich regions of Mn cations, Mn-O-Mn interactions, other rich regions in Mn-O-B'-O-Mn interactions and additional rich regions of B' diamagnetic cations. Indeed, the magnetization loops measured for the Zr- and Hf-based perovskites show

similar behaviour to those observed for spin-glass systems, where a nonlinear behaviour appears with small or negligible hysteresis.[40, 41]

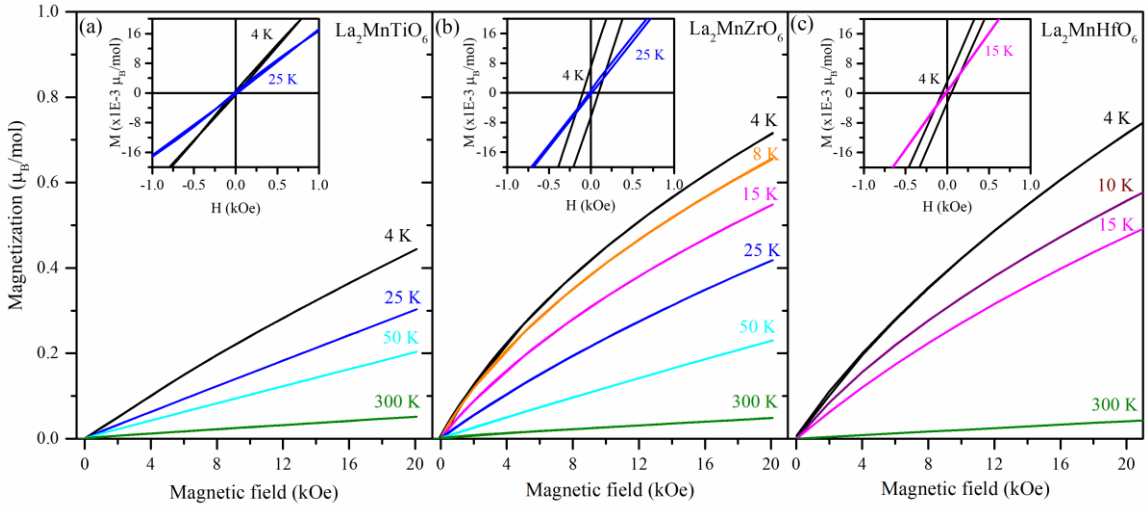

Figure 5. First quadrant of the M vs H curves for perovskites with B' as **(a)** Ti, **(b)** Zr and **(c)** Hf. The corresponding insets show close-up views of the complete hysteresis loops in the low-field region at selected temperatures, below and above T_N.

The magnetic structure analysis of $La_2MnB'O_6$ (B'= Ti, Zr and Hf) has been carried out from a set of NPD patterns, sequentially collected from RT to 1.7 K with a wavelength of λ= 2.52 Å. On the basis of the collected neutron diffraction data, the symmetries observed at RT are retained down to 1.7K.

As it is shown in **Figure 6** (and in the heat map displayed in **Figure S7** in SI), for La_2MnTiO_6 some additional reflections that can be indexed with the propagation vector k = [0 ½ ½] appear below T_N = 9 K, which reveals the existence of long-range magnetic ordering. In **Figure S7** in the SI a small additional reflection at around 28° in 2θ below 130 K can also be observed, which keeps the same intensity down to 1.7 K and it is not indexed with the propagation vector found with respect to the monoclinic unit-cell in the Ti-based perovskite. After a very careful search of other propagation vectors with respect to the monoclinic unit-cell of the perovskite, we realised that this diffraction peak corresponds to the magnetic ordering of the secondary phase MnO. The MnO concentration in the Ti-based perovskite is about 0.5 % and its presence is not detected in the XRPD patterns collected at 300 K (see **Figure S2** in SI). Therefore, we were able to identify this impurity in the compound by means of its long-range magnetic ordering detected with NPD. This reflection is denoted with an asterisk in the pattern measured at 1.7 K, shown in **Figure 6a**.

The magnetic symmetry was analysed by means of the web-based tools ISODISTORT[30] and the Bilbao Crystallographic Server.[34] The space group $P2_1/n$ has only one magnetic irreducible representation (Irrep) associated with k= [0 ½ ½] which is the two-dimensional complex representation mE1+E2+, whose magnetic space group is P_{S-1} (number 2.7) with basis = {(-1, 0, 0),(0, -1, 1),(0, 2, 0)} and origin = (-½, ½, 0). The corresponding Rietveld refinement using this magnetic model is shown in **Figure 6b**, denoting the excellent agreement between the experimental and theoretical patterns. The refinements were performed using one single magnetic and nuclear phase. Due to the low-resolution of the data collected at low-temperature (λ= 2.52 Å in D1B high-flux, low-resolution), we only refined the cell parameters and the components of the magnetic moments and the rest of the parameters were constrained to those values obtained at RT. The refined values of the magnetic parameters are reported in **Table 3** and the mcif file obtained after the refinement is included as a separate file in the SI material. Besides the symmetry constraints imposed by the magnetic space group, further constraints were imposed during the last steps of the refinement, as suggested by the behaviour of

some parameters on achieving the convergence. In particular M_x, M_y and M_z of the two independent Mn sites approaching similar values during the refinement were constrained to be equal.

The refined magnetic model consisting of AFM coupling in the *a*-*c* plane and FM parallel to the *b*-axis is displayed in **Figure 6c**. As shown in this figure, all magnetic moments lie in the *a*–*b* plane, with a small deviation from the *c*-axis. **Table 3** shows that the refined net magnetic moment obtained for Mn^{2+} is in agreement with the expected from 2S= 5 μ_B. The inset of **Figure 6b** shows the thermal evolution of the magnetic moments.

As we mentioned before, two types of magnetic interactions are present in a double perovskite with diamagnetic B' cations: J_{NN} and J_{NNN} (see **Figure 1**).[14] There are three possible AFM orderings depending on the strengths of J_{NN} and J_{NNN}, which are Type-I (J_{NN} >>> J_{NNN}), Type-II (J_{NN} < J_{NNN}) and Type-III (J_{NN} > J_{NNN}).[14] The magnetic structure we obtain for La_2MnTiO_6 corresponds to the AFM Type-II structure, which means the J_{NNN} are the dominant superexchange interactions in the system. A recent study[42] shows that diamagnetic d^{10} and d^0 B' cations have a significant effect on the magnetic interactions in these materials. They demonstrated that d^0 B' cations (for instance Ba_2MnWO_6[42]) promote NNN interactions and therefore the system adopts the AFM Type-II structure. In contrast, d^{10} B' cations (like Ba_2MnTeO_6[42]) promote NN interactions and AFM Type-I magnetic structures. This is because the unfilled d^0 states hybridize strongly with the 2p states of the oxygen, generating NNN extended superexchange interactions that promote an important J_{NNN} in comparison to the J_{NN}.[42] Therefore, the AFM Type-II magnetic structure we obtained for La_2MnTiO_6, where the B' cation is Ti^{4+} -that is d^0-, is in perfect agreement with the results published recently in this article.

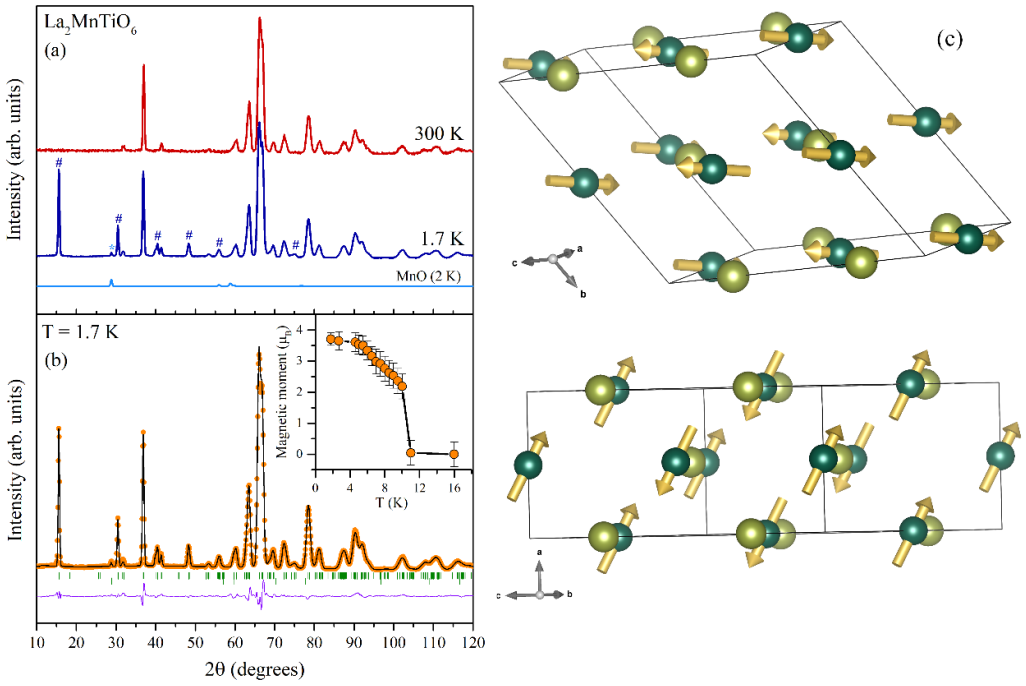

Figure 6. La_2MnTiO_6 perovskite: **(a)** Comparison of NPD data collected at 300K and 1.7 K. The blue # symbols in the pattern at 1.7 K indicate the reflections corresponding to the magnetic ordering for the perovskite phase and the light blue * symbols correspond to the magnetic reflections of MnO. The NPD pattern of MnO measured at 2 K is also shown. **(b)** Refinement obtained with the P_{s-1} magnetic model using NPD data collected at 1.7 K. The second set of vertical green bars corresponds to the crystal and magnetic reflections of unreacted MnO. The inset shows the thermal variation of the refined magnetic moments. **(c)** Schematic representations of the magnetic structure obtained for La_2MnTiO_6 at 1.7 K.

Table 3: Magnetic information obtained from Rietveld refinement using the NPD data collected at 1.7 K for La_2MnTiO_6. See the mcif file in the SI for further details.

Atom site	M_x (μ_B)	M_y (μ_B)	M_z (μ_B)	|M| (μ_B)
Mn1	3.4(1)	1.4(3)	-0.8(2)	3.8(2)
Mn2	3.4(1)	1.4(3)	-0.8(2)	3.8(2)
Magnetic space group		P_{s-1} (number 2.7)		
Propagation vector		(0 ½ ½)		
a (Å)		5.6013(2)		
b (Å)		9.7641(4)		
c (Å)		11.3960(4)		
α (°)		125.480(3)		
β (°)		89.831(9)		
γ (°)		90.286(6)		
R_p		3.04		
R_{wp}		4.25		
R_{exp}		0.23		
R_{Bragg}		5.76		

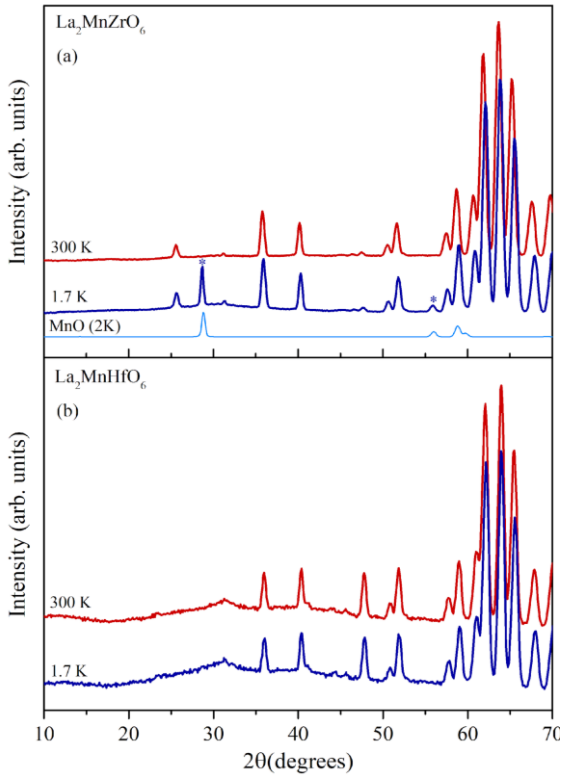

Figure 7. NPD data at 300 K and 1.7 K for **(a)** La_2MnZrO_6 and **(b)** La_2MnHfO_6. In **(a)** the MnO pattern collected at 2 K is also shown. The blue * in the pattern at 1.7 K indicate the magnetic reflections of the unreacted MnO.

For the perovskite La_2MnHfO_6, no additional magnetic reflections were observed below T_N. In the case of the Zr-based sample, some small additional reflections were observed below 130 K (see **Figure 7a** and the heat map displayed in **Figure S8** in SI) that were assigned to magnetic reflections of small amounts of the impurity MnO, similarly to the Ti-based sample. It is worth mentioning that the amount of this phase in the sample is less than 1% and, as in the Ti-based compound, it was not possible to identify the MnO in the XRPD patterns collected at 300 K. Additionally, for La_2MnZrO_6 a diffuse magnetic scattering broad peak is observed at ~ 30º in 2θ, which is the 2θ value where in the Ti analogue (See **Figure 6a** and **6b**) there is a quite

intense magnetic reflection. This might be showing short-range magnetic interactions which are consistent with the irreversibility between the ZFC and FC curves below T_N shown in **Figure 4,** and are responsible for the spin-glass-like behaviour.

A schematic summary of the main results obtained in this work can be found in the phase diagram displayed in **Figure 8**. It is worth noting the major role of the ASD in determining the magnetic behaviour of the three studied new perovskites.

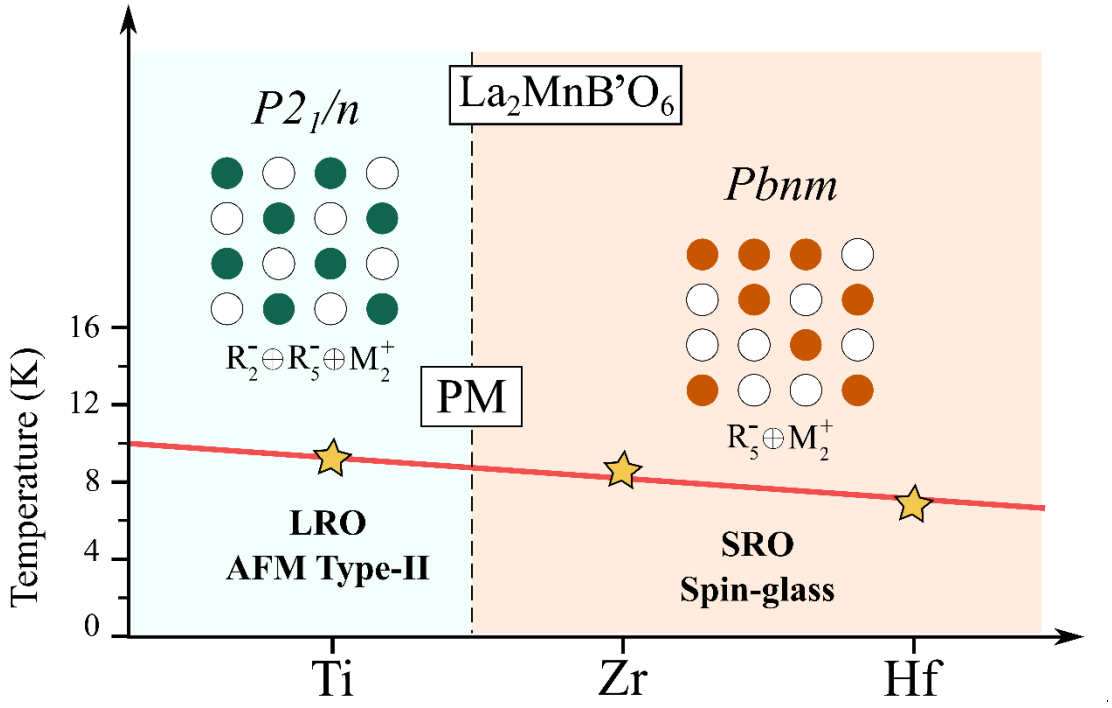

Figure 8. Schematic phase diagram for $La_2MnB'O_6$ (B'= Ti, Zr and Hf), summarising the main structural and magnetic properties found in this work. PM: paramagnetic region; AFM: antiferromagnetic ordering; LRO: long-range order and SRO: short-range order. The yellow stars correspond to the T_N for each compound and the coloured and white spheres are the Mn and B' cations in $La_2MnB'O_6$, respectively. The primary order parameters of the hypothetical phase transition from the high-symmetry *Pm-3m* perovskite for each compound are shown. The *x*-axis denotes the change of the B' cation in the series.

Conclusion

To the best of our knowledge, we are the first to have successfully synthesised the new family of perovskites $La_2MnB'O_6$ (B'= Ti, Zr and Hf), using a conventional solid-state chemistry method, including MnO excess in the formulation. La_2MnTiO_6 crystallizes in the $P2_1/n$ space group with an $a^-a^-c^+$ octahedral tilting and complete rocksalt order of the B-site cations, whereas La_2MnZrO_6 and La_2MnHfO_6 crystallize in the *Pbnm* space group with the same octahedral tilting pattern but with a total anti-site disorder of the cations in B sites. The difference observed in the ordering of the B-site cations might be explained by the radii difference between the Mn and B' cations in this family of perovskites. Slightly more distorted structures were observed in La_2MnZrO_6 and La_2MnHfO_6 than in La_2MnTiO_6.

Clear antiferromagnetic transitions are observed at T_N = 9 K for B'= Ti and Zr, and T_N = 7 K for B'=Hf, but only the Ti-based compound displays long-range magnetic ordering. The crystalline and magnetic structures of La_2MnTiO_6 were very well described by the P_{S-1} magnetic space group and the spins arrangement corresponds to an AFM Type-II structure, where the magnetic interactions between the next-nearest-neighbours Mn cations are stronger than those for the nearest-neighbour cations. The magnetic behaviour observed in La_2MnZrO_6 and La_2MnHfO_6 below the transition temperature is consistent with a spin-glass-like

ordering of the magnetic moments and it is understood by the structural disorder and the competition between the different superexchange interactions in the systems which render strong spins frustration.

Acknowledgments

The authors thank the *Fondo para la Investigación Científica y Tecnológica* (FONCYT) for Project PICT-2016-2495 and the *Secretaria de Ciencia y Tecnología de la Universidad Nacional de Cordoba* (SECyT-UNC) Res. 99/19. The authors thank Dr. Claire Colin from UGA, CNRS, Institut Néel for measuring some of the magnetic curves presented in this work. DMAJ acknowledges a fellowship from CONICET. The authors thank ILL (Grenoble, France) for making all facilities available and 2FDN (*Fédération Française de Diffusion Neutronique*) for the CRG time granted. FP would like to thank Dr. M. S. Senn for the very helpful discussions about Irreps and symmetry analysis.

References

(1) Hwang, J.; Rao, R. R.; Giordano, L.; Katayama, Y.; Yu, Y.; Shao-Horn, Y. Perovskites in catalysis and electrocatalysis. *Science* **2017,** 358, 751-756.

(2) Liu, H.; Yang, X. A brief review on perovskite multiferroics. *Ferroelectrics* **2017,** 507, 69-85.

(3) Zhu, J.; Liu, G.; Liu, Z.; Chu, Z.; Jin, W.; Xu, N. Unprecedented Perovskite Oxyfluoride Membranes with High-Efficiency Oxygen Ion Transport Paths for Low-Temperature Oxygen Permeation. *Adv. Mater.* **2016,** 28, 3511-3515.

(4) Zhang, Z.; Li, J.; Zhou, W.; Yang, C.; Cao, Q.; D. Wang; Du, Y. Mechanism of enhancement in magnetoresistance properties of manganite perovskite ceramics by current annealing. *Ceram. Int.* **2018,** 44, 3760-3764.

(5) Royer, S.; Duprez, D.; Can, F.; Courtois, X.; Batiot-Dupeyrat, C.; Laassiri, S.; Alamdar, H. Perovskites as Substitutes of Noble Metals for Heterogeneous Catalysis: Dream or Reality. *Chem. Rev.* **2014,** 114, 10292−10368.

(6) Glazer, A. M. The classification of tilted octahedra in perovskites. *Acta Cryst.* **1972,** B28, 3384-3392.

(7) Anderson, M. T.; Greenwood, K. B.; Taylor, G. A.; Poeppelmeier, K. R. B-cation arrangements in double perovskites. *Prog. Solid State Chem.* **1993,** 22, 197-233.

(8) Asai, K. F. K.; Nishimori, N.; Satoh, Y.; Kobayashi, Y.; Mizoguchi, M. Magnetic Properties of $REMe_{0.5}Ni_{0.5}O_3$ (RE=Rare Earth Element, Me = Ni, Co). *J. Phys. Soc. Jpn.* **1998,** 67, 4218.

(9) Sarma, D. D. A new class of magnetic materials: Sr_2FeMoO_6 and related compounds. *Curr. Opin. Solid State Mater. Sci.* **2001,** 5, 261-268.

(10) Zinenko, V. I.; Zamkova, N. G.; Maksimov, E. G.; Sofronova, S. N. Lattice dynamics and ferroelectric instability in ordered and disordered $PbSc_{1/2}Ta_{1/2}O_3$ and $PbSc_{1/2}Nb_{1/2}O_3$ solid solutions. *J. Exp. Theor. Phys.* **2007,** 105, 617-625.

(11) Battle, P. D.; Gibb, T. C.; Jones, C. W.; Studer, F. Spin-glass behavior in Sr_2FeRuO_6 and $BaLaNiRuO_6$: A comparison with antiferromagnetic $BaLaZnRuO_6$. *J. Solid State Chem.* **1989,** 78, 281-293.

(12) Izumiyama, Y.; Doi, Y.; Wakeshima, M.; Hinatsu, Y.; Oikawa, K.; Shimojo, Y.; Morii, Y. Magnetic and neutron diffraction studies of the ordered perovskite Ba_2NdRuO_6. *J. Mater. Chem.* **2000,** 10, 2364-2367.

(13) Doi, Y.; Hinatsu, Y.; Oikawa, K.; Shimojo, Y.; Morii, Y. Magnetic properties and crystal structures of ordered perovskites $Sr_2TbRu_{1-x}Ir_xO_6$. *J. Mater. Chem.* **2000,** 10, 1731-1735.

(14) Mutch, H.; Mustonen, O.; Walker, H. C.; Baker, P. J.; Stenning, G. B. G.; Coomer, F. C.; Cussen, E. J. Long and short range magnetism in the frustrated double perovskite Ba_2MnWO_6. *Phys. Rev. Materials* **2020,** 4, 014408.

(15) Cussen, E. J.; Vente, J. F.; Battle, P. D.; Gibb, T. C. Neutron diffraction study of the influence of structural disorder on the magnetic properties of Sr_2FeMO_6 (M=Ta, Sb). *J. Mater. Chem.* **1997,** 7, 459-463.

(16) Gibb, T. C.; Battle, P. D.; Bollen, S. K.; Whitehead, R. J. Investigation of the Crystal and Magnetic Structure of the Perovskite System Sr_2FeTiO_{6-y} by Mössbauer Spectroscopy and Neutron Diffraction. *J. Mater. Chem.* **1992,** 2, 111-114.

(17) Vasala, S.; Karppinen, M. $A_2B'B''O_6$ perovskites: A review. *Prog. Solid. State Ch.* **2015,** 43, 1-36.

(18) Kamegashira, N.; Kobayashi, M.; Saito, J. Synthesis, crystal structure and some properties of Ln_2MnTiO_6 phases (Ln= Rare earth). *Frontiers of solid state chemistry. Ed: Feng SH, Chen JS. Worlds Scientific* **2002**, 47-52.

(19) Ramanujachary, K. V.; Swamy, C. S. Preparation & characterization of La_2TiMnO_6. *Indian J. Chem.* **1981,** 20A, 96-97.

(20) Xiang, X.-D.; Takeuchi, I. Combinatorial Materials Synthesis. *Dekker, New York (2003)*.

(21) Stenzel, A.; Fähsing, D.; Schütze, M.; Galetz, M. C. Volatilization kinetics of chromium oxide, manganese oxide, and manganese chromium spinel at high temperatures in environments containing water vapor. *Mater. Corros.* **2019,** 70, 1426-1438.

(22) Rietveld, H. M. A Profile refinement method for nuclear and magnetic structures. *J. Appl. Crystallogr.* **1969,** 2, 65-71.

(23) Rodríguez-Carvajal, J. Recent advances in magnetic structure determination by neutron powder diffraction. *Phys. B Condens. Matter* **1993,** 192, 55-69.

(24) Evans, J. S. O. Advanced Input Files & Parametric Quantitative Analysis Using Topas. *Mater. Sci. Forum* **2010,** 651, 1-9.

(25) Momma, K.; Izumi, F. VESTA 3 for three-dimensional visualization of crystal, volumetric and morphology data. *J. Appl. Cryst.* **2011,** 44, 1272-1276.

(26) Limandri, S.; Robledo, J.; Tirao, G. Extracting chemical information from high-resolution Kβ X-ray emission spectroscopy. *Spectrochim. Acta B* **2018,** 144, 29-37.

(27) Shannon, R. D. Revised effective ionic radii and systematic studies of interatomic distances in halides and chalcogenides. *Acta Crystallogr. A* **1976,** 32, 751-767.

(28) Blanco, M. C.; De Paoli, J. M.; Ceppi, S.; Tirao, G.; Nassif, V. M.; Guimpel, J.; Carbonio, R. E. Synthesis, structural characterization and magnetic properties of the monoclinic ordered double perovskites $BaLaMSbO_6$, with M = Mn, Co and Ni. *J. Alloys Compd.* **2014,** 606, 139-148.
(29) Patterson, A. L. The Scherrer formula for X-ray particle size determination. *Phys. Rev.* **1939,** 56, 978-982.
(30) Campbell, B. J.; Stokes, H. T.; Tanner, D. E.; Hatch, D. M. ISODISPLACE: a web-based tool for exploring structural distortions. *J. Appl. Crystallogr.* **2006,** 39, 607-614.
(31) Howard, C. J.; Kennedy, B. J.; Woodward, P. M. Ordered double perovskites- a group-theoretical analysis. *Acta Cryst.* **2003,** B59, 463-471.
(32) Howard, C. J.; Stokes, H. T. Group-Theoretical analysis of octahedral tilting in perovskites. *Acta Cryst.* **1998,** B54, 782-789.
(33) Senn, M. S.; Bristowe, N. C. A group-theoretical approach to enumerating magnetoelectric and multiferroic couplings in perovskites. *Acta Cryst.* **2018,** A74, 308-321.
(34) Perez-Mato, J. M.; Orobengoa, D.; Arroyo, M. I. Mode crystallography of distorted structures. *Acta Cryst.* **2010,** A66, 558-590.
(35) Aimi, A.; Mori, D.; Hiraki, K.; Takahashi, T.; Shan, Y. J.; Shirako, Y.; Zhou, J.; Inaguma, Y. High-Pressure Synthesis of A-Site Ordered Double Perovskite $CaMnTi_2O_6$ and Ferroelectricity Driven by Coupling of A-Site Ordering and the Second-Order Jahn−Teller Effect. *Chem. Mater.* **2014,** 26, 2601-2608.
(36) Inaguma, Y.; Aimi, A.; Shirako, Y.; Sakurai, D.; Mori, D.; Kojitani, H.; Akaogi, M.; Nakayama, M. High-Pressure Synthesis, Crystal Structure, and Phase Stability Relations of a $LiNbO_3$-Type Polar Titanate $ZnTiO_3$ and Its Reinforced Polarity by the Second-Order Jahn−Teller Effect. *J. Am. Chem. Soc.* **2014,** 136, 2748-2756.
(37) Lufaso, M. W.; Woodward, P. M. Jahn-Teller distortions, cation ordering and octahedral tilting in perovskites. *Acta Cryst.* **2004,** B60, 10-20.
(38) Ok, K. M.; Halasyamani, P. S. Distortions in Octahedrally Coordinated d^0 Transition Metal Oxides: A Continuous Symmetry Measures Approach. *Chem. Mater.* **2006,** 18, 3176-3183.
(39) Lakshminarasimhan, N.; Nanda Kumar, A. K.; Selva Chandrasekaran, S.; Murugan, P. Structure-magnetic property relations in $FeNbO_4$ polymorphs: A spin glass perspective. *Prog. Solid. State Ch.* **2019,** 54, 20-30.
(40) Kumar, A.; Pandey, D. Study of magnetic relaxation, memory and rejuvenation effects in the cluster spin-glass phase of B-site disordered $Ca(Fe_{1/2}Nb_{1/2})O_3$ perovskite: Experimental evidence for hierarchical model. *J. Magn. Magn.* **2020,** 511, 166964.
(41) Kumar, A.; Senyshyn, A.; Pandey, D. Evidence for cluster spin glass phase with precursor short-range antiferromagnetic correlations in the B-site disordered $Ca(Fe_{1/2}Nb_{1/2})O_3$ perovskite. *Phys. Rev. B* **2019,** 99, 214425.
(42) Mustonen, O. H. J.; Pughe, C. E.; Walker, H. C.; Mutch, H. M.; Stenning, G. B. G.; Coomer, F. C.; Cussen, E. J. Diamagnetic d-Orbitals Drive Magnetic Structure Selection in the Double Perovskite Ba_2MnTeO_6. *Chem. Mater.* **2020,** 32, 7070-7079.

SUPPLEMENTARY INFORMATION

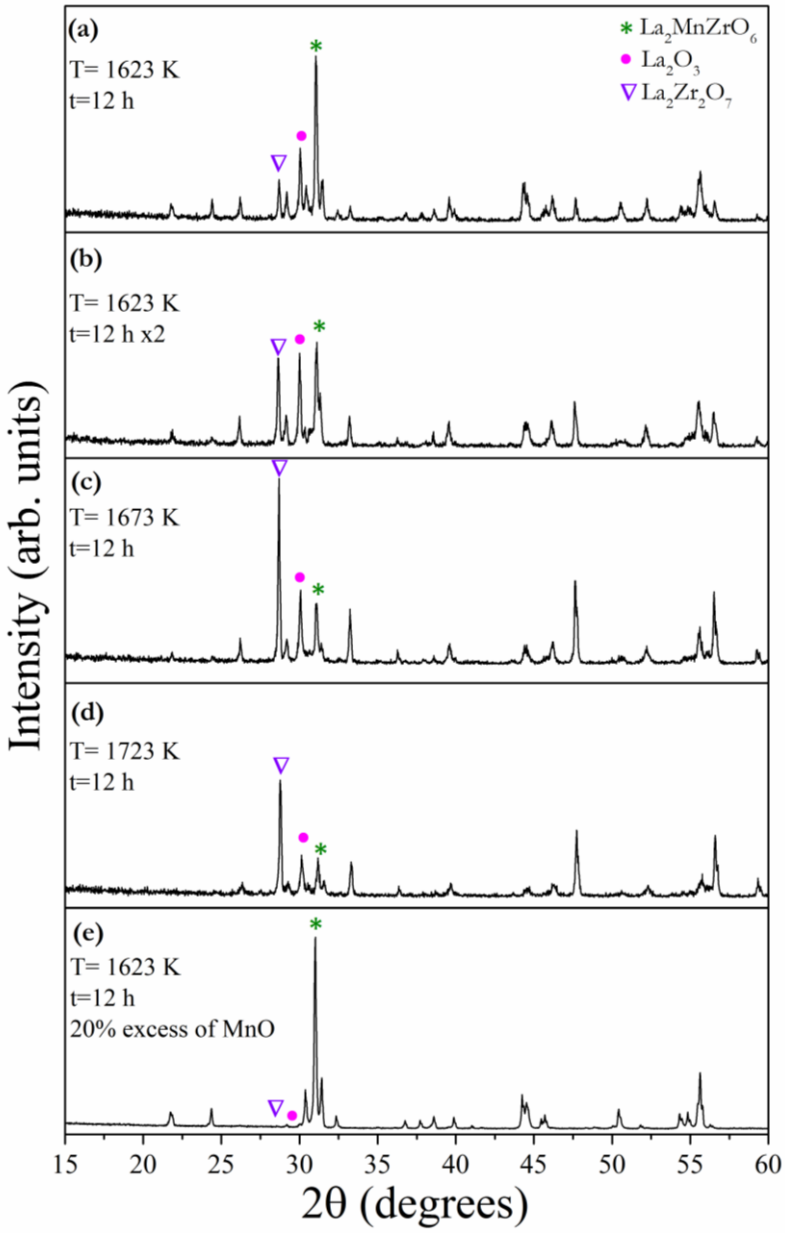

Figure S1: X-ray powder diffraction (XRPD) patterns for different syntheses conditions to obtain the Zr-based perovskite. The conditions used for the syntheses performed with stoichiometric quantities of the regents were: **(a)** 1623 K during 12 h, **(b)** same sample as (a) heated again to the same temperature for 12 h more, **(c)** 1673 K during 12 h and **(d)** 1723 K during 12 h. **e)** Synthesis performed with 20% MnO excess at 1623K during 12 h. The impurities obtained are marked with symbols.

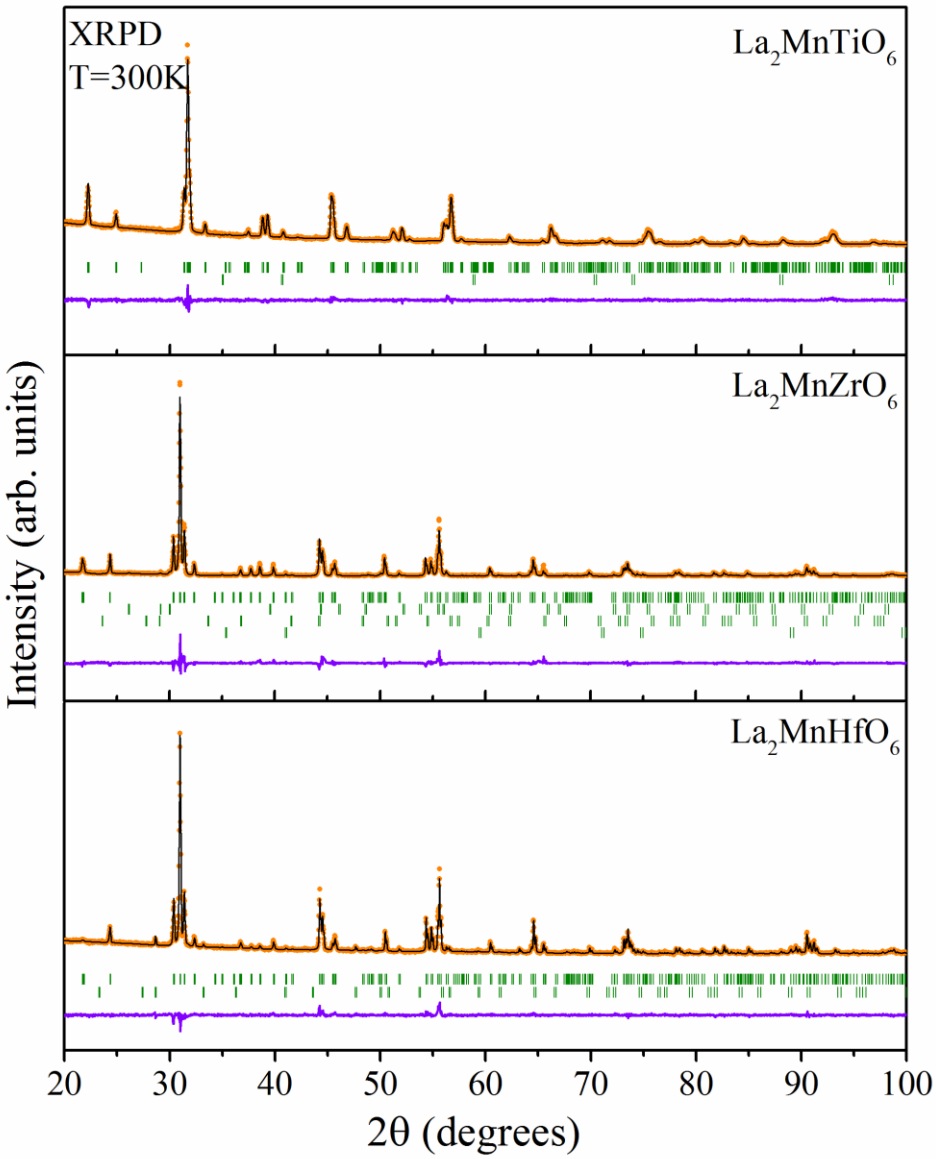

Figure S2: Refined XRPD patterns collected at 300K for B'= Ti, Zr and Hf. Observed (orange dots), calculated (black full line), Bragg reflections (vertical green bars) and difference (violet bottom line). The first set of Bragg reflections corresponds to the main perovskite phase. The second phase for the Ti-based perovskite corresponds to unreacted MnO. For the Zr-based perovskite, the second, third and fourth reflections correspond to La_2O_3, $La_2Zr_2O_7$ and MnO, respectively. For the Hf-based perovskite the second reflections correspond to $La_2Hf_2O_7$. The MnO phase in B' = Zr and Ti was added to the refinements of the XRPD patterns after the detection of this phase in the neutron powder diffraction (NPD) data collected at low temperature, as it is explained in the main text.

Table S1. Atomic coordinates, thermal parameters and occupancies for the whole family of perovskites after Rietveld refinement from NPD data at 300 K. The abbreviation *Occ* indicates the occupation of each crystallographic site in the unit cell.

B'	**Space group**	**Ion**	***Site***	***x***	***y***	***z***	B_{iso} **(Å^2)**	***Occ***
Ti	$P2_1/n$	La	4*e*	0.01086(1)	0.04464(2)	0.24936 (2)	0.46(2)	0.98(1)
		Mn/Ti	2c	0.5	0	0.5	0.17(3)	0.01(1)/0.99 (1)
		Mn/Ti	2b	0.5	0	0	0.45(3)	0.99 (1)/0.01 (1)
		O1	4e	0.30566 (1)	0.71847 (2)	0.04854 (1)	0.74(2)	0.999(1)
		O2	4e	0.71768(2)	0.30672(2)	0.54168(1)	0.74(2)	0.999(1)
		O3	4e	-0.08598(1)	0.52287(1)	0.26037(2)	0.74(2)	0.976(1)
Zr	*Pbnm*	La	4*c*	0.01053(3)	-0.05198(2)	0.25	1.13(2)	0.99(1)
		Mn/Zr	*4b*	0.5	0	0	1.99(2)	0.52(1)/0.48(1)
		O1	*8d*	0.69865(2)	0.30086(2)	-0.05315(2)	0.92(2)	0.99(1)
		O2	*4c*	0.89920(3)	0.53694(3)	0.25	0.92(2)	0.99(1)
Hf	*Pbnm*	La	4*c*	0.01223(1)	-0.05416(2)	0.25	1.02(2)	0.98(1)
		Mn/Hf	*4b*	0.5	0	0	1.19(4)	0.51(1)/0.49(1)
		O1	*8d*	0.69994(3)	0.29929(4)	-0.05302(2)	1.15(2)	0.99(1)
		O2	*4c*	0.89974(2)	0.53237(3)	0.25	1.15(2)	0.99(1)

Table S2. Comparison of the Irreps's notation with the different settings for the high symmetry perovskite parent structure.

A 1*b* (½ ½ ½) B 1*a* (0 0 0) X *3d* (½ 0 0)	**A 1*a* (0 0 0) B 1*b* (½ ½ ½) X *3c* (0 ½ ½)**
R_5^+ - La(a)	**R_4^- - La(a)**
R_5^+ - La(b)	R_4^- - La(b)
X_5^+ - La	**X_5^- - La**
R_5^+ - O(a)	R_4^- - O(a)
R_5^+ - O(b)	R_4^- - O(b)
X_5^+ - O	**X_5^- - O**
R_1^+ - O	**R_2^- - O**
R_4^+ - O	**R_5^- - O**
M_3^+ - O	**M_2^+ - O**
R_3^+ - O	R_3^- - O
M_2^+ - O	M_3^+ - O
M_5^+ - O	M_5^+ - O

Table S3. Refined bond distances B/B'-O, angles (θ) B-O-B' and tilt angles (δ) at RT for the whole family of perovskites. For B'= Zr and Hf: *Site1*=*Site2*= Wyckoff site *4b*. For B'= Ti: *Site1* and *Site2* are *2b* and *2c* Wyckoff sites respectively. The tilting angle of the octahedrons were calculated as δ= (180-θ)/2.

B'		Distances (Å) $(B/B')_{site1}$-O	Distances (Å) $(B/B')_{site2}$-O	θ (°)	δ (°)
	O1	1.978(3) x2	2.155(3) x2	150.7(1)	14.6
Ti	O2	1.958(3) x2	2.159(3) x2	152.6(1)	13.7
	O3	1.975(5) x2	2.134(5) x2	151.8(2)	14.1
	Average	1.9703	2.149	151.7	14.1
	O1	2.122(3)x4		147.25(2)	16.37
Zr	O2	2.123(4)x2		146.40(1)	16.80
	Average	2.122		146.83	16.59
	O1	2.122(3)x4		147.70(2)	16.15
Hf	O2	2.121(4)x2		147.02(2)	16.49
	Average	2.122		147.36	16.32

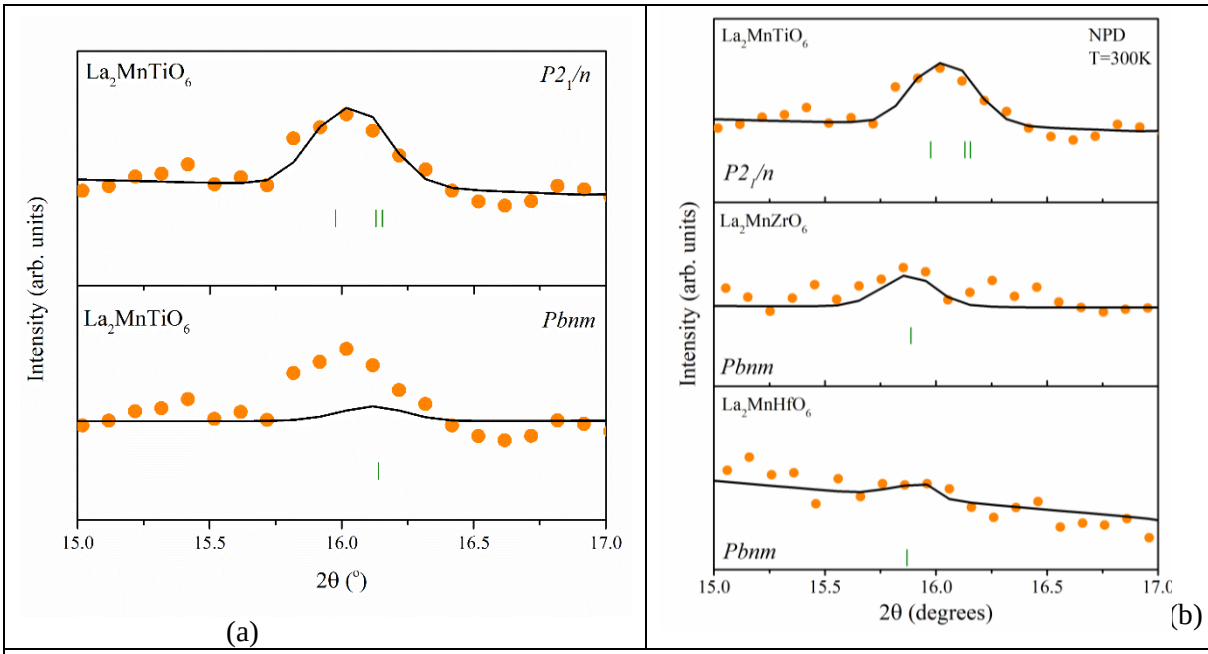

Figure S3: Close-up view of the Rietveld refinements in the low-angle region for: **(a)** Ti-based perovskite with *P2₁/n* and *Pbnm* models and **(b)** all the studied compounds.

The measured spectra with normalized intensity are shown in **Figure S4a**, where it can be seen that the Kβ' intensity decreases, indicating that the oxidation state of Mn increases, in agreement with previous reports.[1] The fitting obtained is displayed in **Figure S4b**. In order to quantify the oxidation state of Mn, the intensity Kβ' relative to the total intensity of the Kβ region (I-Kβ') was used. From the corresponding fittings, the oxidation state of Mn for the perovskite was determined by considering the linear fit displayed in **Figure S4c**. From this analysis, it was obtained that the average oxidation state of Mn in the perovskite $La_{0.99(1)}Mn_{0.52(1)}Zr_{0.48(1)}O_{3.00}$ is (2.10 ± 0.11), which is in very good agreement with the value obtained from the analysis of NPD data.

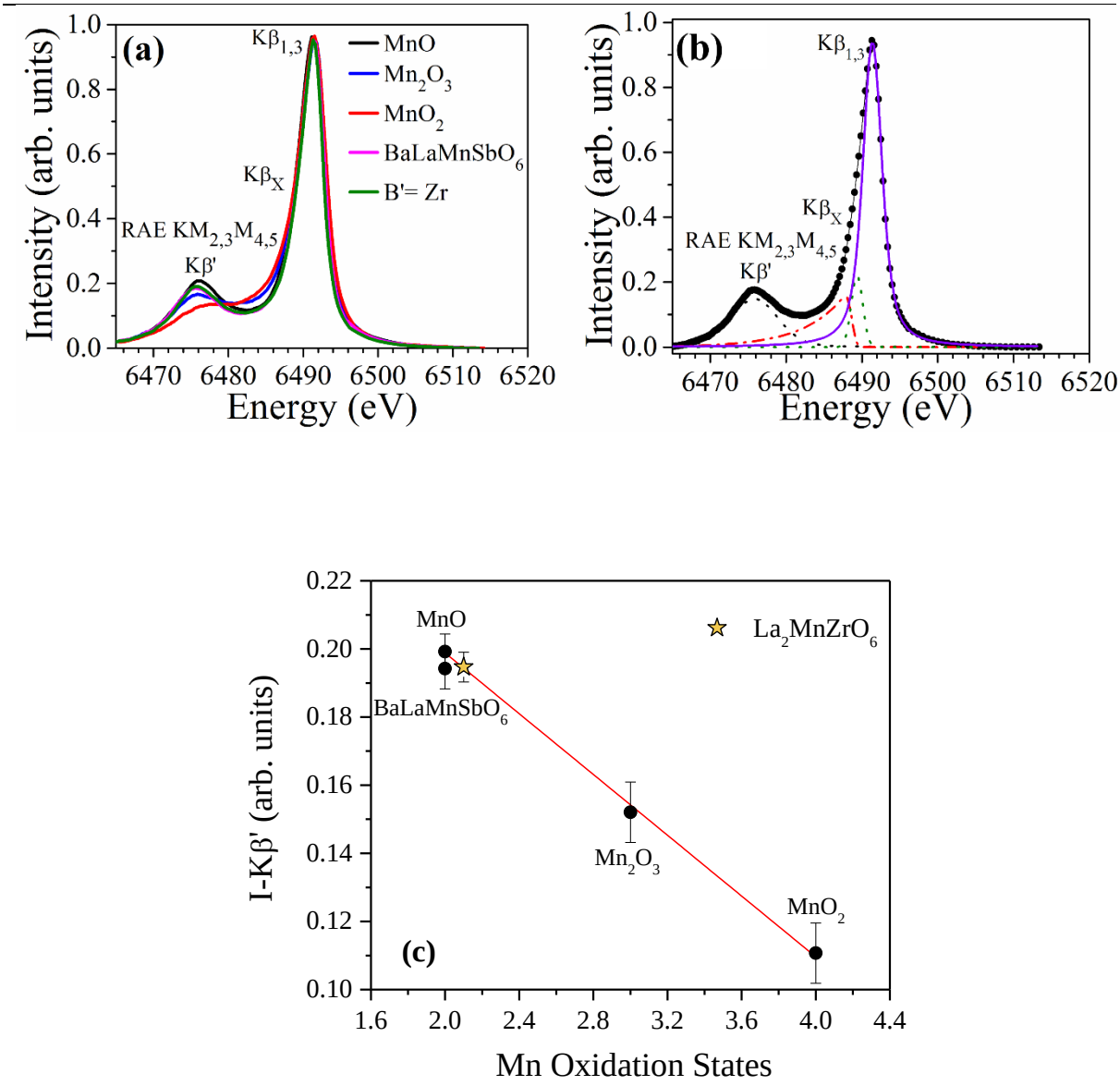

Figure S4: **(a)** Kβ' emission spectra for La_2MnZrO_6 together with the spectra for the Mn reference samples. **(b)** Experimental spectra with the respective fit for B'= Zr. Dots: experimental data; continuous and dotted lines: fitted curve and the corresponding individual contributions of the Voigt functions (Kβ', $K\beta_X$ and $K\beta_{1,3}$ peaks) and EMG (RAE $KM_{2,3}M_{4,5}$ transition). **(c)** Intensity of the Kβ' (I- Kβ') line as a function of the oxidation states of the Mn for the prepared perovskite with B'= Zr.

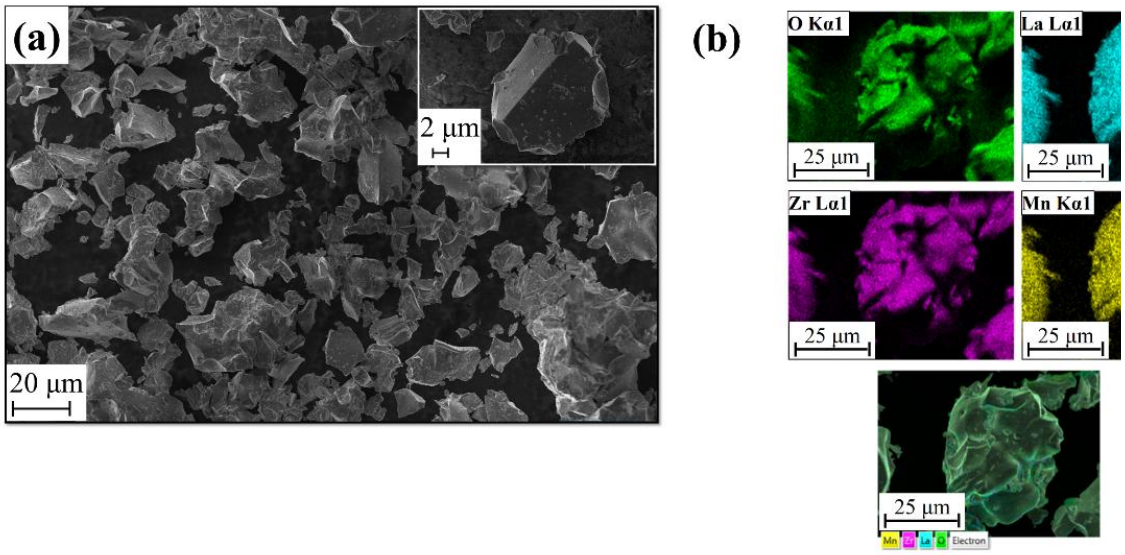

Figure S5: La_2MnZrO_6 shown as a representative example for the whole family **(a)** Scanning electron microscopy images and **(b)** Elemental EDS maps.

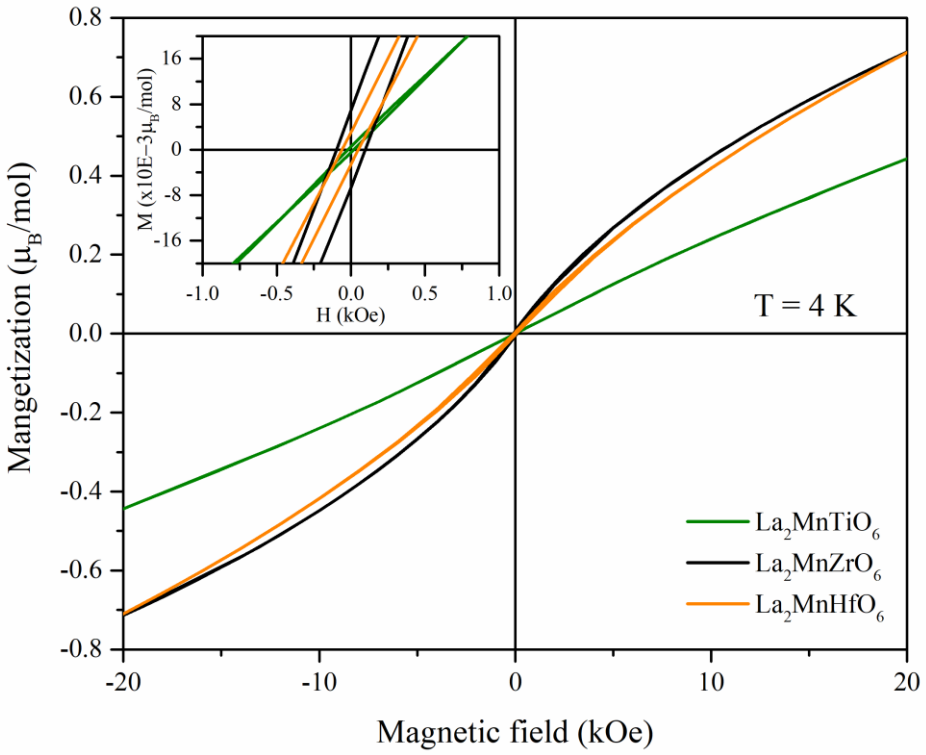

Figure S6: M vs H hysteresis loops for $La_2MnB'O_6$ (B'= Ti, Zr and Hf) measured at 4 K. The inset is a close-up view of the low-field region.

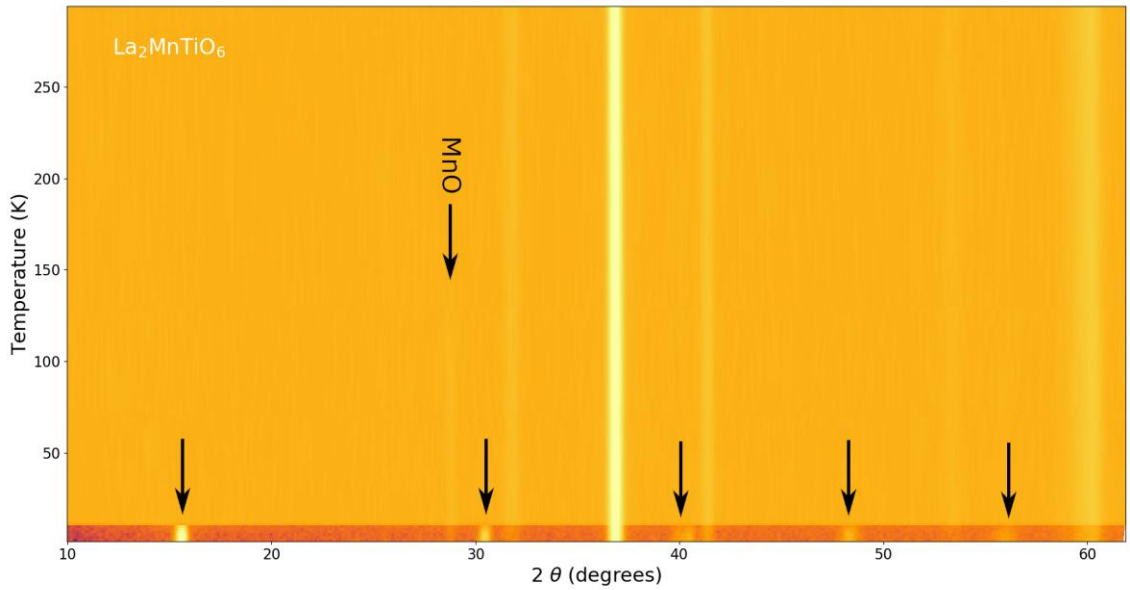

Figure S7: Heat map of NPD data for the Ti-based perovskite. The arrows correspond to the peaks of the magnetic phase.

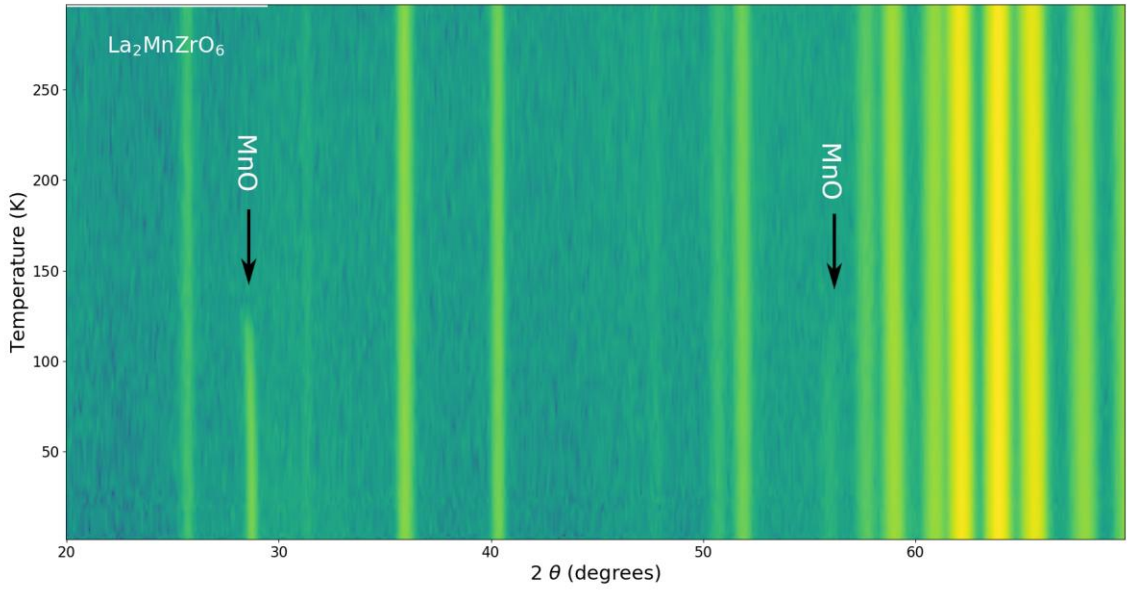

Figure S8: Heat map of NPD data for Zr-based perovskite. The arrows correspond to the magnetic reflections of the unreacted MnO.

Crystallographic Data (Powder)			
Source (laboratory X-ray, synchrotron, neutron time of flight (TOF), neutron constant wavelength)	Neutron powder constant wavelength	Neutron powder constant wavelength	Neutron powder constant wavelength
Chemical formula	La_2MnTiO_6	La_2MnZrO_6	La_2MnHfO_6
Formula Weight (g/mol)	476.60	519.92	607.19
Temperature (K)	300	300	300
Pressure (if not ambient)	Ambient	Ambient	Ambient
Wavelength for constant wavelength (NPD) (Å)	1.28	1.28	1.28
Crystal system	Monoclinic	Orthorhombic	Orthorhombic
Space group (No.)	14	62	62
a, b, c, α, β, γ	5.6130(3) 5.7006(3) 7.9724(5) 90.0 89.93(1) 90.0	5.6930(3) 5.8831(3) 8.1313(5) 90.0 90.0 90.0	5.6992(3) 5.8799(3) 8.1381(4) 90.0 90.0 90.0
V ($Å^3$)	255.10(3)	272.34(3)	272.71(4)
Z	2	4	4
d-space range (Å)	0.80-6.0	0.80-6.0	0.80-6.0
χ^2 (NPD)	47.12	57.55	49.31
R_p (NPD)	7.01	6.06	6.82
R_{wp} (NPD)	6.59	6.60	6.32
Definition of R factors			
$\chi^2=(1/N)\Sigma_i(y_{C,i}-y_{O,i})^2/\sigma^2[y_{O,i}]$			
$R_{wp}{}^2=\Sigma_i w_i(y_{C,i}-y_{O,i})^2/\Sigma_i w_i(y_{O,i})^2$			

(1) Tsutsumi, K.; Nakamori, H.; Ichikawa, K. X-ray Mn Kb emission spectra of Manganese oxides and manganates. *Phys. Rev. B* **1976,** 13, 929-933.